frontiers | Frontiers in Tropical Diseases

TYPE Original Research
PUBLISHED 25 October 2022
DOI 10.3389/fitd.2022.1016426

OPEN ACCESS

EDITED BY
Laurent Marsollier,
Institut National de la Santé et de la Recherche Médicale (INSERM), France

REVIEWED BY
Azger Dusthackeer,
National Institute of Research in Tuberculosis (ICMR), India
Saad Alghamdi,
Umm al-Qura University, Saudi Arabia

*CORRESPONDENCE
Shelley E. Haydel
Shelley.Haydel@asu.edu

†PRESENT ADDRESS
John Popovich,
Department of Anesthesiology, Rush University, Chicago, IL, United States
Shaojiang Chen,
Intel Corporation, Chandler, AZ, United States

SPECIALTY SECTION
This article was submitted to Neglected Tropical Diseases, a section of the journal Frontiers in Tropical Diseases

RECEIVED 10 August 2022
ACCEPTED 26 September 2022
PUBLISHED 25 October 2022

CITATION
Dermody R, Ali F, Popovich J, Chen S, Seo D-K and Haydel SE (2022) Modified aluminosilicates display antibacterial activity against nontuberculous mycobacteria and adsorb mycolactone and *Mycobacterium ulcerans in vitro*. *Front. Trop. Dis.* 3:1016426. doi: 10.3389/fitd.2022.1016426

Modified aluminosilicates display antibacterial activity against nontuberculous mycobacteria and adsorb mycolactone and *Mycobacterium ulcerans in vitro*

Roslyn Dermody[1], Farizah Ali[2], John Popovich[3†], Shaojiang Chen[2†], Dong-Kyun Seo[2] and Shelley E. Haydel[1,3*]

[1]School of Life Sciences, Arizona State University, Tempe, AZ, United States, [2]School of Molecular Sciences, Arizona State University, Tempe, AZ, United States, [3]The Biodesign Institute Center for Bioelectronics and Biosensors, Arizona State University, Tempe, AZ, United States

Mycobacterium ulcerans (MU) infection of skin and soft tissue leads to chronic skin ulceration known as Buruli ulcer. MU releases a lipid-like toxin, mycolactone, that diffuses into the tissue, effecting disease through localized tissue necrosis and immunosuppression. Cutaneous Buruli ulcer wounds slowly advance from a painless pre-ulcerative stage to an ulcerative lesion, leading to disparities in the timing of medical intervention and treatment outcomes. Novel Buruli ulcer wound management solutions could complement and supplement systemically administered antimicrobials and reduce time to healing. Capitalizing on nanopore structure, adsorption, and exchange capacities, aluminosilicate nanozeolites (nZeos) and geopolymers (GPs) were developed and investigated in the context of therapeutics for mycobacterial disease ulcerative wound care. nZeos were ion exchanged with copper or silver to assess the antimicrobial activity against MU and *Mycobacterium marinum*, a rapid growing, genetic ancestor of MU that also causes skin and soft tissue infections. Silver- and copper-exchanged nZeos were bactericidal against MU, while only silver-exchanged nZeos killed *M. marinum*. To mediate adsorption at a biological scale, GPs with different pore sizes and altered surface modifications were generated and assessed for the ability to adsorb MU and mycolactone. Macroporous GPs with and without stearic acid modification equivalently adsorbed MU cells, while mesoporous GPs with stearic acid adsorbed mycolactone toxin significantly better than mesoporous GPs or GPs modified with phenyltriethoxysilane (PTES). In cytotoxicity assays, Cu-nZeos lacked toxicity against Detroit 551, U-937, and WM-115 cells. GPs demonstrated limited cytotoxicity in Detroit 551 and WM-115, but produced time-dependent toxicity in U-937 cells. With their large surface area and adsorptive capacities, aluminosilicates nZeos and GPs may be modified and developed to support conventional BU wound care. Topical application of nZeos and GPs could kill MU within the cutaneous wound

10.3389/fitd.2022.1016426

environment and physically remove MU and mycolactone with wound dressing changes, thereby improving wound healing and overall patient outcomes.

KEYWORDS

mycobacteria, *Mycobacterium ulcerans*, *Mycobacterium marinum*, aluminosilicates, antimicrobial ions, silver, copper, adsorption

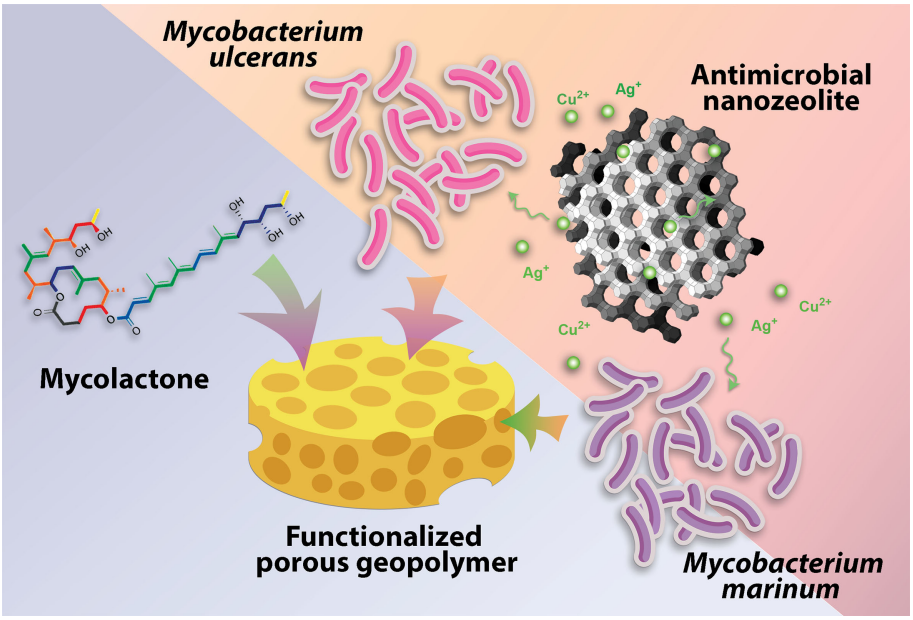

GRAPHICAL ABSTRACT

Introduction

Buruli ulcer is a painless, progressive skin and soft tissue infection (SSTI) caused by *Mycobacterium ulcerans* (MU) (1). Cases of this neglected tropical disease are observed in equatorial countries, wherein disease occurrence is associated with proximity to wetlands and bodies of water (2, 3). Infection manifests as a diminutive nodule, wherein the lengthy MU replicative cycle yields protracted ulceration (3, 4). MU accumulates in the subcutaneous extracellular space (5) and secretes the polyketide toxin mycolactone (6, 7), generating cytopathic analgesia (8). The resulting painlessness prompts benign negligence of the wound, condoning bacterial penetration of underlying tissue (9). As in the case of latent *Mycobacterium tuberculosis*, deferred treatment of Buruli ulcer compromises therapeutic efforts (10, 11).

A fully oral regimen of rifampicin and clarithromycin by the World Health Organization has greatly advanced treatment of Buruli ulcer (12). However, success of this regimen is confined to early cases of the disease (13, 14). Despite indications of antibiotic susceptibility *in vitro*, parenteral antibiotic therapies must account for penetration of the infection site (12). Localized treatment, as utilized in the care of other SSTIs, supports greater therapeutic access to the wound (15). Evidence of the antimicrobial activity of clay materials against MU (16) has garnered interest as an alternative to conventional small molecule compounds (1, 17). Aluminosilicate materials, a group of modulated clay derivatives, provide a versatile framework for topical therapeutic delivery (18).

Our research team created two synthetic, customized aluminosilicates – nanozeolites (nZeos) and geopolymers (GPs) – to mimic clay's predominant antimicrobial features: ion content (19) and adsorption (20), respectively (21–23), and to ensure consistency, safety, and efficacy of developed products for treating SSTIs (24). Ion-exchanged nanozeolites (IE-nZeos)

and GPs strategically exploit ion release and adsorptive capacities for leveraging topical therapeutic applications with site-directed antimicrobial delivery and bacterial and toxin adsorption, respectively, as we previously demonstrated (21–23). Metal ions with previously reported antimicrobial properties, such as copper and silver (16, 25), can be interchangeably attached to the extensive nZeos surface, enabling subsequent ion exchange with water or moisture and dispersion of metal ions from the scaffold into the environment (22, 23, 26).

Mycobacterium marinum (Mmar), the closest genetic relative of MU and a fast-growing nontuberculous mycobacterium SSTI pathogen (27–30), causes non-ulcerative granulomatous skin lesions that are often linked with fish aquaria (31) or fishing-related injuries (32). As a close relative of both MU and *Mycobacterium tuberculosis* (33), Mmar provides context to decades of research focused on ion-dependent antimicrobial activity against mycobacteria (25, 34, 35). Silver nanoparticles exhibit antimicrobial activity against Mmar (35), whereas silver enriched dressings (36, 37) and copper-rich clay materials (16) kill MU. Jointly, these findings suggest the pertinence of IE-nZeos as intermediates for mycobacterial wound care.

Geopolymers (GPs), amorphous counterparts to zeolites, are aluminosilicate materials that can be customized to control porosity, physicochemical properties, and functionality (18, 38, 39). The porous structure of these compounds adsorbs heavy metals and industrial manufacturing waste (18). In a biomedical context, we recently demonstrated that porous GPs adsorb whole bacterial cells, toxins, and other secreted products (21, 22). Given that Buruli ulcer pathology is largely ascribable to mycolactone secretion and activity (6, 40), sequestration of either (a) mycolactone alone or (b) whole MU cells is expected to vastly improve disease prognosis (41). GPs have significant technological potential due to ease and low cost of production (38), making GPs exceptional candidates for use in endemic MU areas with minimal healthcare infrastructure (3). With high mechanical and chemical stabilities, GPs can be functionalized by coating the surface with operative agents and/or moieties that impart specific physicochemical properties (42).

To assess the antimicrobial activity of nZeos against SSTI-associated mycobacteria, we investigated *in vitro* antimicrobial activity of copper and silver nZeos against MU and Mmar (43). Based on pore size capacities and our previous GP adsorption studies with bacterial cells and toxins (21), macroGPs were tested for the adsorption of MU cells and mesoGPs were assessed for mycolactone adsorption. To impart GPs with heightened hydrophobicity, the surface of GP materials was modified with stearic acid (saturated fatty acid) or phenyltriethoxysilane (PTES) (a silane coupling agent with hydrophobic characteristics). These steric acid-coated GPs (SA-GPs) or PTES-coated GPs (PTES-GPs) were predicted to display greater lipophilic or hydrophobic behavior than their uncoated counterparts (44). As a result, we expected that these surface-modified GPs would bind apolar mycolactone (45) and lipid-rich MU (46) with increased affinities.

Materials and methods

Synthesis and characterization of Ag-nZeos and Cu-nZeos

The synthesis and characterization of Ag-nZeos and Cu-nZeos were reported previously (22, 23). In short, nZeos were prepared by heating a Na-based geopolymer resin with the nominal composition of $3.0Na_2O$: $1.0Al_2O_3$: $4.0SiO_2$: $32.4H_2O$, which was mixed homogeneously with canola oil. The precursors for the geopolymer resin were NaOH pellets (Sigma Aldrich), water glass (Sigma Aldrich), metakaolin (MetaMax® from BASF), and deionized (DI) water. The oil reduces the alkalinity of the reaction mixture during heating, thereby improving the zeolitic crystallinity of the final product. The zeolite product was washed repetitively with DI water until the pH of the filtrate reached about 8. Ag-nZeos and Cu-nZeos were prepared by exchanging Na^+ ions in nZeos with Ag^+ and Cu^{2+} ions, respectively. To exclude the nZeos as a source of antimicrobial activity, nZeo carriers were enriched with sodium (Na-nZeos) (22). For characterization of chemical structures and morphologies, powder X-ray diffraction (PXRD) patterns, scanning electron microscopy (SEM) images, and transmission electron microscopy (TEM) of dried samples were collected on Siemens D5000 powder X-ray diffractometer, XL30 environmental FEG microscope and Titan 80-300 FEG-TEM (FEI Co., Hillsboro, OR), respectively.

Brunauer-Emmett-Teller (BET) surface areas were estimated with a Micrometrics ASAP 2020 volumetric adsorption analyzer with nitrogen as the adsorbate at 77 K. Prior to the analysis, samples (approximately 300 mg) were degassed at 300°C for at least 6 h under a vacuum until a residual pressure of ≤10 µm Hg was reached. Specific surface areas were determined from the BET equation. The *t*-plot method was used to distinguish the contributions from micropores (pore size: < 2 nm) and from the mesopores (pore size: from 2 nm to 50 nm) to the pore volume (the combined volume of micropores and mesopores) and surface area. The mesopore volumes were calculated after subtracting the micropore volume from the total pore volume. Pore size distributions were obtained using the Barrett-Joyner-Halenda (BJH) method assuming a cylindrical pore model from the desorption branch of sorption isotherms (47). Elemental compositions of the zeolite samples were determined by combining Rutherford backscattering and particle induced X-ray emission data. The hydrodynamic

particle size of the nZeos sample was measured on Malvern Nano-ZS instrument with a helium neon laser.

Synthesis and characterization of macroporous and mesoporous GPs

The synthesis and characterization of macroporous and mesoporous GPs were reported previously (21). For macroporous GPs, the synthetic process resembles nZeos preparation. Fumed silica (4.15 g) (Cabot, CA-BO-SIL® EH-5; aggregate particle size: 0.2 – 0.3 μm; primary size: 5 -25 nm) was added to 12.0 mL of KOH (11.6 *M*) solution and mechanically mixed (IKA® RW 60 digital mixer) at 800 rpm for 30 min to dissolve the silica. Metakaolin [7.64 g (Metamax, BASF; average particle size: 1.3 μm)] was added to the solution and the mixture was stirred again at the same speed for 40 min to form a homogenous fluidic liquid. Paraffin oil (Alfa Aesar, Haverhill, MA) was then added to the resin at a 1:1 oil-to-water volume ratio and stirred under the same mixing condition for 15 min, resulting in a homogeneous, viscous emulsion. After heating at 60°C for 24 h, the cured monolithic product was crushed into small pieces (1 – 2 mm) and subjected to Soxhlet extraction with hexane as the solvent. The product was washed extensively with DI water until a neutral pH was achieved (pH ~7) and dried in a lab oven overnight at 90°C.

For mesoporous GPs, an aluminosilicate precursor mixture with a composition of $3.1K_2O$: Al_2O_3: $5.5SiO_2$: $66H_2O$ was prepared by first adding 6.05 g of KOH pellets and 18.03 g of potassium silicate solution (PQ corporation, H_2O: 60.8 wt%, K_2O: 12.65 wt%, SiO_2: 26.55 wt%) in 14.55 mL of DI water in a cold bath. Once the KOH pellets were dissolved, the solution was brought to room temperature and mixed with 5.09 g of the metakaolin. Stirring with the mechanical mixer at 800 rpm for 40 min produced a visually homogeneous and free-flowing geopolymer resin. The resin was transformed into a paste by heating the resin at 90°C for 6 h in a sealed 50 ml polypropylene tube. To isolate the solid component, the paste was subjected to repetitive washings with DI water, followed by centrifugation at 6000 rpm (g-force: ~2500 m/s^2) for 15 min, until the supernatant was pH ~8. After drying at 90°C overnight, the resulting powder product was stored in sealed glass vials at room temperature.

The chemical structures and morphological features of all the samples were examined by collecting PXRD patterns and SEM/TEM images. Brunauer-Emmett-Teller (BET) surface area analysis was performed using a Micrometrics ASAP 2020 volumetric adsorption analyzer with nitrogen as the adsorbate at 77 K. The *t*-plot method was used to distinguish the micropores from the mesopores in the samples and to calculate the external surface areas. By subtracting the micropore volume from the total pore volume, mesopore volumes were calculated. Mesopore size distributions were obtained using the Barrett-Joyner-Halenda (BJH) method assuming a cylindrical pore model and calculating the distance between opposite walls of the pore (47).

GP surface modifications to enhance hydrophobicity

As previously described (21), surface modification of the GP products with stearic acid was carried out by an esterification reaction between silanol groups on the surfaces of geopolymers. Stearic acid (0.2 g) was dissolved in 25 mL of 0.6 M NaOH solution in a 90°C water bath. After adding 1.0 g of macroGP or mesoGP to the hot solution, the mixture was magnetically stirred for 10 min at 90°C and slowly cooled to room temperature while agitating. Precipitate products were filtered and washed extensively with DI water to reduce the pH to ~8.0. The products were dried in a lab oven at 60°C overnight and then placed in another oven at 160°C for 4 h to induce crosslinking of carboxylic acid groups to the surface of the geopolymer. Finally, the dried products were washed with hot toluene multiple times to remove unbound stearic acid and then dried again at 60°C overnight. After producing stearic acid-modified macroGPs (SA-macroGPs) and stearic acid-modified mesoGPs (SA-mesoGPs), Fourier transform infrared (FT-IR) spectra were recorded using a Bruker IFS66 V/S attenuated total reflection FT-IR spectrometer. Carbon–hydrogen–nitrogen (CHN) elemental analyses were performed by employing Perkin-Elmer 2400 Series II CHNS/O Analyzer (Waltham, MA) with a thermal conductivity detector.

Phenyltriethoxysilane (PTES)-GPs were prepared with PTES as a surface modifier and motor oil as a pore-forming agent with a 1:1 oil: resin volume ratio. First, 0.96 g of DI water, 0.74 g of NaOH, 12.23 g of water glass (Sigma-Aldrich; SiO_2 27 wt %, NaOH 14 wt %, H_2O 59 wt %), and 1.01 g of PTES (Gelest, Inc., Morrisville, PA) were mixed and stirred with a high-shear mixer at 500 RPM for 10 min. To the mixture solution, 6.17 g of metakaolin was added and stirred at 100 RPM for 30 min. The resulting GP resin was then mixed with 10 mL of motor oil and the liquid mixture was stirred at 800 RPM for 30 min until becoming homogeneous, after which the mixture was heated at 70°C for 24 h in a tightly sealed container. After heating, the resulting hard monolithic solid was crushed into a coarse powder and washed with hexane and then ethanol repetitively to remove the oil from the sample, yielding the PTES-GP sample.

Mycobacterial strains and growth conditions

Cultures of Mmar ATCC 927 and MU 1615 (graciously provided by Dr. Pamela Small, University of Tennessee, Knoxville, TN, USA) were grown in Middlebrook 7H9

supplemented with 0.2% glycerol, 0.05% Tween 80, and 10% oleic acid-dextrose-catalase (OADC), hereafter referred to as M7H9. All liquid cultures were maintained at 30°C with gentle rotation. To produce homogenous bacterial suspensions, clumps were dispersed with 23-gauge needles. Samples were adjusted to an OD_{600} of ~0.3 (~2 x 10^7 cells/ml), then diluted 1:100 prior to experimental use. Middlebrook 7H10 agar plates, designated M7H10, were supplemented with 0.5% glycerol and 10% OADC. To maintain a microaerophilic environment and prevent desiccation, M7H10 plates were sealed and incubated at 30°C. Mmar and MU colony forming units (CFU) were counted after incubation for 1 week or 6 weeks, respectively.

In vitro Mmar IE-nZeos susceptibility testing

A five-day M7H9 broth microdilution susceptibility assay determined sensitivity to metal ions released by IE-nZeos (48). The antimicrobial activity of streptomycin (STR) (4, 8 μg/ml) was analyzed in parallel (48). At 24 h intervals, all experimental wells were sampled. Samples were subsequently diluted and plated on M7H10 and incubated at 30°C for one week. The minimum bactericidal concentration required to reduce the bacterial population by 99% (MBC_{99}) was determined with resultant CFU counts.

In vitro MU IE-nZeos susceptibility testing

To assess the susceptibility of MU to IE-nZeos, two-fold serial dilutions of IE-nZeos (4-128 μg/ml) were incubated with MU for 21 d in M7H9 (48). STR (4 μg/ml) was used as a control for *in vitro* antimicrobial activity. Aliquots were collected at one-week intervals, serially diluted ten-fold in PBS-Tween 80 (0.1% v/v, pH 7), and plated on M7H10 agar. Pursuant to a six-week incubation at 30°C, MBC_{99} was quantified.

In vitro cytotoxicity assays

Representative skin, soft tissue, and immune cells were used to assess the cytotoxicity of Cu-nZeos and GPs, as previously demonstrated with Ag-nZeos (23) Detroit 551 human skin fibroblasts (ATCC CCL-110), WM-115 human skin epithelial cells (ATCC CRL-1675), and U-937 human monocytes (ATCC CRL-1593.2) were propagated according to manufacturer instructions. In 96-well microtiter plates, each cell type was seeded at a density of 3-6 x 10^3 cells per well. Following an overnight attachment period, cells were exposed to two-fold dilutions of Cu-nZeos (128–8 μg/ml) or GPs (10 mg/ml) in 180 μL. Untreated cells served as controls for all independent experimental replicates. After a 24-hour incubation, supernatant was transferred to a black-walled, clear bottom, 96-well microtiter plate, and CellTox Green cytotoxicity reagent (Promega Corporation, Madison, WI) was added to experimental and control wells. Excitation and emission fluorescence was measured in relative fluorescent units (RFUs) with wavelengths of 485 nm and 520 nm, respectively. Cytotoxicity was determined by comparing RFU measurements of control, untreated cells and Cu-nZeo- and GP-treated cells (23).

MU bacterial cell adsorption assays

MacroGPs or SA-macroGPs (10 mg) were added to MU saline suspensions (1 ml). MU-GP mixtures were incubated for 1 h at 30°C with gentle orbital agitation (100 rpm) to prevent sedimentation. MU saline suspensions without the addition of macroGPs were included as untreated controls. To remove GPs and GP-bound MU from solution, all samples (including MU untreated controls), were filtered using a sterile 5-μm cellulose syringe filter. Filtered supernatants containing unbound MU cells were subjected to serial dilutions in PBS-Tween 80 (0.1% v/v) and plated in duplicate on M7H10 agar. After the M7H10 plates were incubated at 30°C for 6 weeks, CFU/ml for each MU-GP co-incubation was determined.

Mycolactone extraction

TLC isolation of mycolactone was performed as previously described from four- to six-week-old MU cultures incubated on M7H10 agar (7, 49). A 2:1 (v/v) chloroform: methanol mixture extracted total lipids from whole cells. The chloroform-soluble fraction was dried and resuspended in ice-chilled acetone. Acetone-soluble lipids were separated on a TLC plate in a solution of 90:10:1 (v/v/v) chloroform: methanol: water. Upon exposure to long wave UV light (365 nm), the yellow band observed at R_f = 0.23 was collected and solubilized in absolute ethanol. Following silica removal with a 0.2 μm PTFE filter, mycolactone was isolated *via* HPLC (50).

Mycolactone toxin adsorption assays

Purified mycolactone (two independent isolates) was adjusted to an OD_{362} of 0.5 in 100% ethanol (51). MesoGPs, SA-mesoGPs, or PTES-GPs (10 mg) were added to mycolactone suspensions (~25 mg per 1 ml). Untreated mycolactone solutions were analyzed in parallel. To minimize photodegradation (51) and evaporation of the mycolactone suspension, samples were incubated in amber vials for 1 h at

room temperature. Thereafter, samples were briefly centrifuged (100 RPM) to sediment GP particles. To determine the level of remaining mycolactone, we analyzed the absorbance (Λ_{max} = 362 nm) of each sample in a quartz cuvette (Hellma, Müllheim, Germany). GP-treated, 100% ethanol-only samples were measured to detract background signal. The final mycolactone concentration was subtracted from the starting concentration to determine the amount adsorbed by GPs.

Statistical analyses

We assessed statistical significance using Welsh's t-tests for normally distributed data, Mann-Whitney U tests for data reflecting non-normal distributions, and ANOVA with Brown-Forsythe test and Welsh's correction. All statistical analyses were conducted using GraphPad Prism 9 software (San Diego, CA, United States). Samples with a difference of $p < 0.05$ were regarded significant.

Results

Characteristics and properties of modified aluminosilicate nZeo materials

Synthesis and detailed characteristics of nZeos, Ag-nZeos, Cu-nZeos, macroGPs, mesoGPs, and SA-mesoGPs were described previously (21–23, 26). In summary, nZeos, Ag-nZeos, and Cu-nZeos are 100 to 700 nm-sized aggregates composed of intergrown zeolite nanocrystals with lateral dimensions of 20 – 40 nm. Textual pores between the aggregated nanocrystals revealed a hierarchical pore structure with both zeolitic micropores and mesopores to the aggregates. Their PXRD patterns indicated formation of faujasite-type structures. From the elemental analysis, the silver and copper loadings for Ag-nZeos and Cu-nZeos were estimated to be 24 and 8.3 wt% (2.2 and 1.3 mmol/g), respectively (23, 26).

Characteristics and properties of modified aluminosilicate GP materials

The PXRD patterns of macroGPs and mesoGPs (21) showed that both are non-crystalline geopolymeric materials (52). After modification with SA, the PXRD patterns of SA-macroGPs and SA-mesoGPs resembled their parent materials, indicating that geopolymer structure was not affected by the surface modification experiments. The macroGPs exhibited discrete spherical pores with pore diameters in the range of 50 – 200 µm, with additional smaller pores ranging from 200 – 500 nm on the pore walls (21). The smaller pores are due to the nanoscopic biphase formation between the inorganic geopolymer component and the organic paraffin oil component. The much larger spherical pores coexist after the biphase formation due to excess paraffin oil remaining in the mixture as large oil droplets. After curing the GP component, oil extraction leaves the two types of pore structures in the product. As expected, the SA-macroGPs and SA-mesoGPs exhibit the same morphology as the parent macroGPs and mesoGPs, respectively, indicating that surface modification does not change the morphology of the inorganic geopolymer (21). Meanwhile, the mesoGPs form aggregates composed of strongly interconnected primary nanoparticles of 20 – 30 nm in diameter with apparent textural porosity (21). BJH analyses revealed that the average pore size of mesoGPs was 31 nm due to the presence of textural porosity observed in the TEM studies (23). Meanwhile, macroGPs exhibit large pore sizes in the range of 50 – 200 µm and 200 – 500 nm with a small number of mesopores with an average pore size of 26 nm (21).

Characterization of the PTES-GPs using SEM imaging and N_2 gas sorption studies revealed both spherical macropores and mesopores walls (Figure 1), indicating similarity with macroGPs (21, 26). SEM imaging revealed PTES-GPs with seemingly discrete spherical pores with pore diameters in the range of in the 2 – 50 µm (Figures 1A, B). From N_2 gas sorption analysis (Figure 1C), the total surface area was 44.1 m^2/g, while the BJH analysis revealed a 12 nm of average pore size and estimated 0.13 cm^3/g of mesopore volume (Figure 1D). Colorimetric titration with methylene blue indicated that only 0.7% of the total surface area could absorb the cationic dye molecules, proving a strong hydrophobic surface for PTES-GPs (data not shown).

In vitro nZeos activity against Mmar is ion specific

Since Mmar is susceptible to silver nanoparticles [Ag^+ equivalency of 1 µg/ml (35)], we subjected Mmar to *in vitro* antimicrobial susceptibility assays with Ag-nZeos. At the 5-day experimental endpoint, 64 µg/ml Ag-nZeos (Ag^+ equivalency of 15.36 µg/ml (23); Table 1) reduced Mmar ≥100 fold, indicating MBC_{99} bactericidal activity similar to the streptomycin antibiotic controls (Figure 2A). In the presence of Ag-nZeos (32-256 µg/ml), Mmar viability decreased from 0 to 3 days with CFU levels subsequently remaining static through day 5 (Figure 2A). Conversely, Cu-nZeos (4-128 µg/ml) did not affect Mmar viability (Figure 2B). All tested concentrations of Na-nZeos (16-128 µg/ml) grew synchronously with the Mmar growth control (Figure 2C), indicating the innocuous nature of nZeos carriers. Cumulatively, these results indicate that silver released from Ag-nZeos is responsible for the Mmar antimicrobial activity observed.

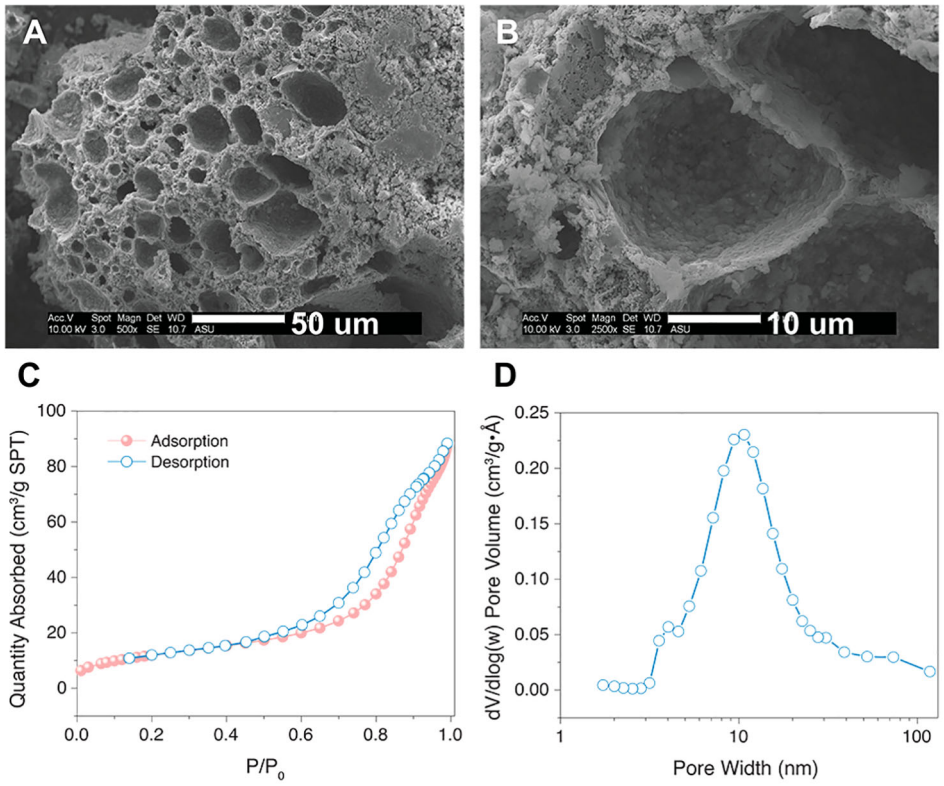

FIGURE 1
(A) Low-magnification and **(B)** high-magnification SEM images of PTES-GPs. Scale bar = 50 µm **(A)**, 10 µm **(B)**. **(C)** N_2 gas sorption isotherm and **(D)** BJH pore size distribution of PTES-GPs.

TABLE 1 nZeos antimycobacterial activity and ion equivalency.

nZeos	Mmar MBC_{99} (µg/ml)	Mmar MBC_{99} Ion equivalence (µg/ml)	MU MBC_{99} (µg/ml)	MU MBC_{99} Ion equivalence (µg/ml)
Ag-nZeos	64	15.36 Ag^+	16	3.84 Ag^+
Cu-nZeos	N/A	N/A	32	2.69 Cu^{2+}

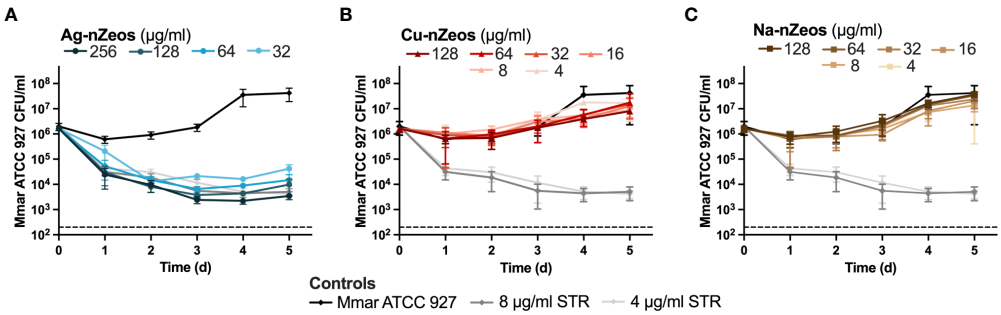

FIGURE 2
IE-nZeos antimicrobial activity against Mmar is ion specific. Mmar was exposed to two-fold dilutions of **(A)** Ag-nZeos (256 – 32 µg/ml), **(B)** Cu-nZeos (128 – 4 µg/ml), **(C)** Na-nZeos (128 – 4 µg/ml), and **(A, B, C)** STR (8 – 4 µg/ml) for 5 d. Viability was assessed by plating samples at 1 d intervals. Each point represents the triplicate sample mean (SD). The assay limit of detection is demarcated by the hatched line at 200 CFU/ml.

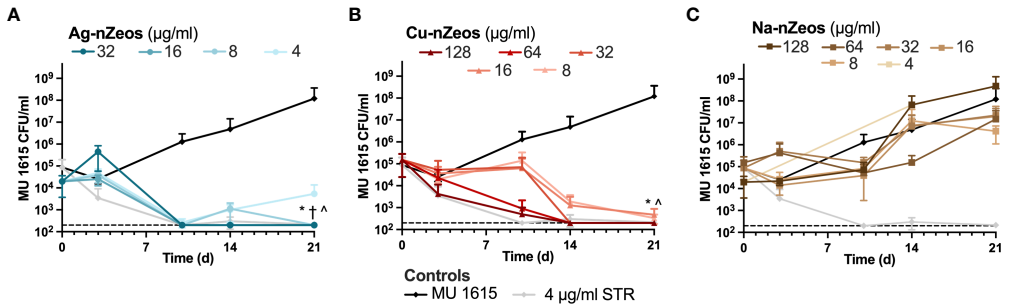

FIGURE 3
Ag-nZeos and Cu-nZeos kill MU. MU 1615 was exposed to two-fold dilutions of **(A)** Ag-nZeos (32 – 4 µg/ml), **(B)** Cu-nZeos (128 – 8 µg/ml), **(C)** Na-nZeos (128 – 4 µg/ml), and **(A, B, C)** streptomycin (STR; 4 µg/ml) with CFU viability assessed at 3, 10, 14 and 21 d. Each point represents the triplicate sample mean (SD). The assay limit of detection is demarcated by the hatched line at 200 CFU/ml. *32 µg/ml, †16 µg/ml; ^8 µg/ml with $p < 0.05$; Ag- and Cu-nZeos were compared to corresponding concentrations of Na-nZeos.

Antimicrobial activity of nZeos against MU

Having demonstrated ion specificity and the ability of Ag-nZeos to kill Mmar, we sought to examine the relative ion species-specific antimicrobial activity of nZeos against MU. Similar to STR, ≥4 µg/ml Ag-nZeos (Ag^+ equivalency of 0.96 µg/ml (23); Table 1) reduced MU to the limit of detection, revealing the MBC_{99} by the 10 d time point (Figure 3A). Cu-nZeos enacted antimicrobial activity in a protracted manner, whereby 32 µg/ml Cu-nZeos (Cu^{2+} equivalency of 2.69 µg/ml (22); Table 1) was observed as the MBC_{99} at 14 d (Figure 3B). MU co-incubated with Na-nZeos (4-128 µg/ml) demonstrated no significant difference ($p > 0.05$) from the untreated control (Figure 3B), corroborating the innocuous character of nZeo carriers. The concentration- and time-dependent antimicrobial activity of Ag- and Cu-nZeos against MU reflects ion-specific mechanisms of action. IE-nZeos indicate proximity-based bactericidal activity which reflects the potential of aluminosilicates as topical therapeutic agents.

Cytotoxicity assessment of Cu-nZeos

We previously determined that nZeo carriers lack toxicity against eukaryotic cells (23). Furthermore, Chen et al. (23) demonstrated an Ag-nZeos LC_{50} of 64 µg/ml against Detroit 551 and WM-115 cells, whereas U-937 cell viability was not

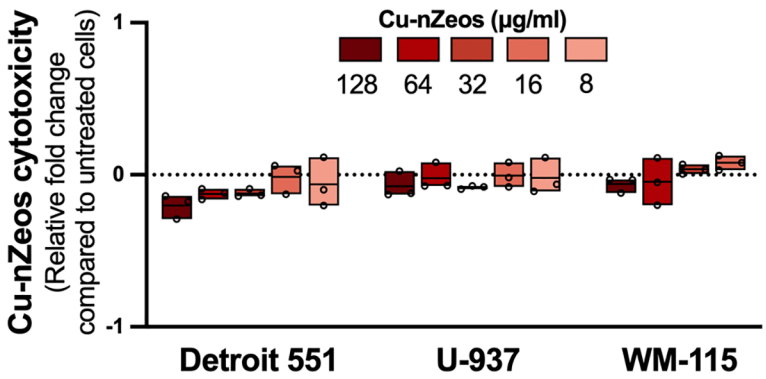

FIGURE 4
Cu-nZeos lack mammalian cell cytotoxicity. Detroit 551, U-937, and WM-115 mammalian cells were exposed to Cu-nZeos (8 – 128 µg/ml) for 24 h, followed by cell viability measurements, as outlined in materials and methods. Data are represented as the relative fold change in excitation/emission fluorescence values between Cu-nZeo experimental samples and untreated cells. Values for individual replicates are flanked by floating box plots, wherein the mean of each experimental group is represented as a line. The dotted line represents the normalized value for untreated cells and the fold-change threshold for Cu-nZeo experimental replicates.

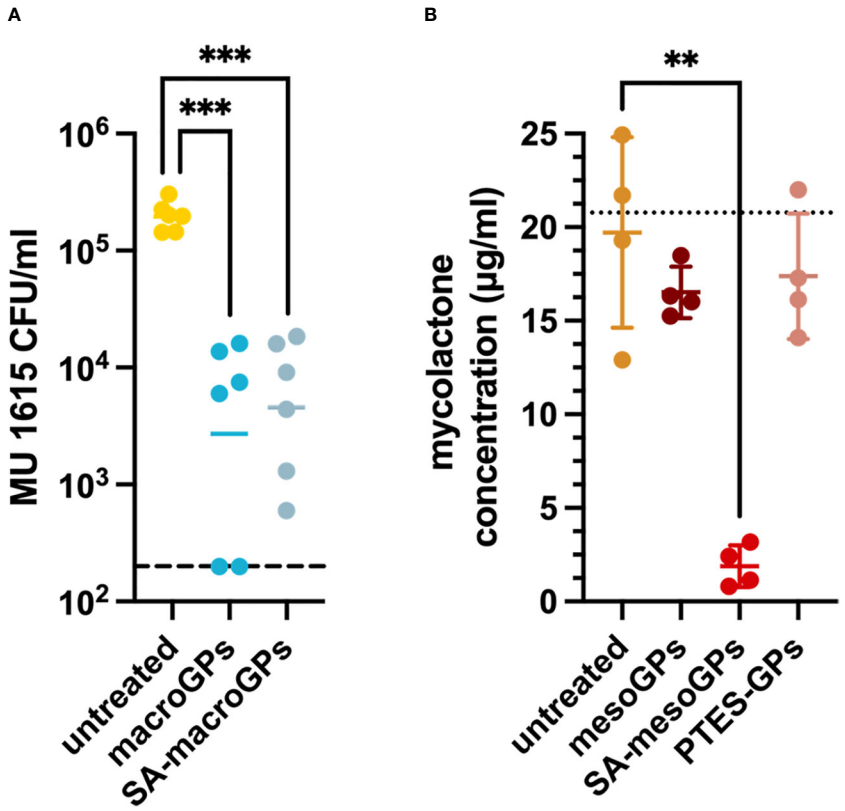

FIGURE 5
Geopolymers adsorb MU bacteria and mycolactone toxin. **(A)** MU 1615 cells were incubated with macroGPs (10 mg/ml) or SA-macroGPs (10 mg/ml) for 1 hour at 30°C. Each point represents a single technical replicate collected from triplicate samples with geometric mean. Experimental limit of detection **(A)** is indicated by a hatched line at 200 CFU/ml. **(B)** Mycolactone (~20 mg) was incubated with mesoGPs (10 mg/ml), SA-mesoGPs (10 mg/ml), or PTES-GPs (10 mg/ml) for 1 hour at room temperature. Each point represents a single technical replicate collected from duplicate samples with mean (SD). The dotted line corresponds to mycolactone concentration prior to experimental incubation. ***$p < 0.001$; ANOVA test with Brown-Forsythe test and Welsh's correction to compare GP-treated and untreated MU samples. **$p < 0.01$; Welsh's t-test comparing GP-treated samples to untreated mycolactone samples.

affected by Ag-nZeos at any tested concentration (2 - 128 µg/ml). To establish the potential host toxicity, Cu-nZeos-associated mammalian cell lysis was measured in the same three eukaryotic cells: Detroit 551 human skin fibroblasts, U-937 human monocytes, and WM-115 dermal epithelial cells. Compared to untreated cells, Cu-nZeos lacked cytotoxicity against Detroit 551, WM-115, and U-937 cells at or above the biologically relevant concentration (32 µg/ml) that killed MU (Figures 4, 3B). These results indicate that nZeos effect differential toxicity in bacterial and mammalian cells.

MacroGPs and SA-macroGPs sequester MU cells in suspension

Since macroGPs and SA-macroGPs adsorb MRSA (21), we sought to determine if these GPs could physically adsorb and remove MU cells in suspension. MU bacterial suspensions were incubated with macroGPs or SA-macroGPs for 1 h, and nonadherent MU cells were quantified. A single application of macroGPs or SA-macroGPs (10 mg/ml) adsorbed ≥95% of MU cells (Figure 5A). Surface-modification with SA, a saturated fatty acid, to heighten hydrophobicity did not enhance binding to lipid-rich MU (Figure 5A). Nevertheless, these findings further support the role of macroGPs as immuring and adsorptive agents of bacteria that cause cutaneous infections.

SA-mesoGPs effectively bind mycolactone

Throughout the course of infection, MU secretes the polyketide toxin mycolactone. Much of the pathology observed in Buruli ulcer has been ascribed to the broad range of mycolactone cytotoxicity, suggesting that toxin removal

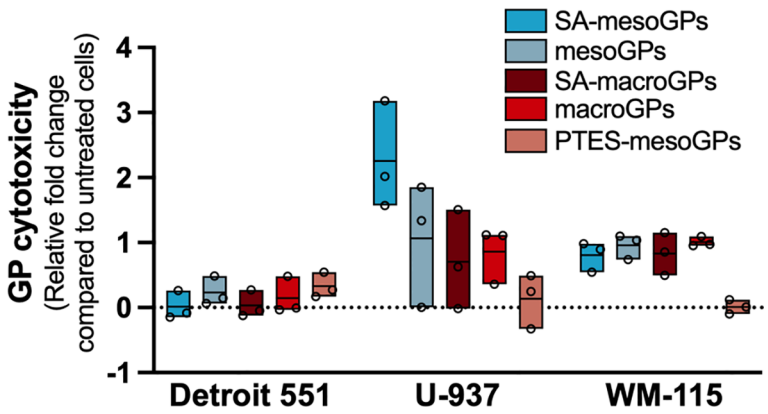

FIGURE 6
Cytotoxicity assessment of geopolymers. Detroit 551, U-937, and WM-115 mammalian cells were exposed to GPs (10 mg/ml) for 24 h, followed by cell viability measurements, as outlined in materials and methods. Data are represented as the relative fold change in excitation/emission fluorescence values between GP experimental samples and untreated cells. Values for individual replicates are flanked by floating box plots, wherein the mean of each experimental group is represented as a line. The dotted line represents the normalized value for untreated cells and the fold-change threshold for GP experimental replicates.

restores immune function at the infection site (40). In our previous studies, GPs adsorb diverse bacterial toxins, including α-hemolysin and streptolysin O (21). Due to greater hydrophobicity, we hypothesized that SA-mesoGPs and PTES-GPs would adsorb greater quantities of mycolactone than their uncoated counterpart. Mycolactone remaining in solution was regarded as unbound. SA-mesoGPs (10 mg/ml) neared total adsorption (92.8%) of the initial amount of mycolactone (~20 mg) (Figure 5B). In contrast, mesoGPs adsorbed ~35% of total mycolactone, whereas PTES-GPs adsorbed less than 10% mycolactone (Figure 5B). SA-mesoGPs displayed significant affinity for mycolactone sequestration, indicating that the SA saturated fatty acid plays an important role in hydrophobic interactions with the polyketide mycolactone toxin.

Cytotoxicity assessment of macroGPs and mesoGPs

Cytotoxicity of the GP materials was assessed using Detroit 551, WM-115, and U-937 mammalian cells incubated with GPs (10 mg/ml) for 24 h. The five GP products only minimally decreased viability (0.01 - 0.35-fold) of Detroit 551 human skin fibroblasts compared to untreated cells (Figure 6). Except for PTES-modified mesoGPs, other tested GP materials increased cytotoxicity 0.8 - 1-fold in WM-115 dermal epithelial cells (Figure 6). Compared to untreated samples, U-937 cells exposed to macroGPs and SA-macroGPs for 24 h also exhibited 0.7 – 0.9-fold increases in cytotoxicity (Figure 6). While PTES-mesoGPs had minimal effects on U-937 human monocytes, mesoGPs and SA-mesoGPs exhibited 1- to 2.3-fold increases in cytotoxicity compared to untreated cells (Figure 6). Since macroGPs and SA-mesoGPs significantly adsorbed MU cells (Figure 5A) and mycolactone toxin (Figure 5B), respectively, with 1 h incubations and exhibited minimal cytotoxic effects on skin fibroblasts and epithelial cells with 24 h incubations, these results further support potential wound-adjacent applications for mycobacterial skin and soft tissue infections (53) (Figure 6).

Discussion

Despite an improved standard of care in early Buruli ulcer cases (13, 14), the prognosis for advanced disease remains grim with surgical procedures, such as invasive debridement, frequently necessitated and often delayed (31). Non-small molecule compounds may arbitrate the treatment of advanced cases (13). Modified and customized aluminosilicate materials offer many benefits as potential therapeutics, including low production cost, long-term stability, and ease of application (21–23, 26).

IE-nZeos demonstrated divergent antimicrobial activity against the tested mycobacterial species. While Ag-nZeos killed both Mmar and MU, only MU was susceptible to Cu-nZeos (Figures 2B, 3B). The antimycobacterial activity profile of each nZeos species (Figures 2A, 3A) may stem from physiological differences between species. Though undefined, silver ion antibacterial activity is speculated to result from disruption of the membrane structure, cellular ion gradient (54), and electron transport, whereas copper ions are speculated to metabolic disturbance (55, 56).

The differential identity of Mmar and MU as fast- and slow-growing species, respectively, likely influences susceptibility to ion-based metabolic interference (57). Efflux pump activity imbues mycobacteria with broad-spectrum chemotherapeutic resistance (58). Because of their permissive nature, mycobacterial efflux pumps also hinder intracellular metal ion accumulation and toxicity (59, 60). Greater active transporter activity in Mmar, the fast-growing species, may contribute to the species' copper resistance (61). Host macrophages appear to exploit the copper susceptibility of slow-growing intracellular pathogens, as in the case of *Mycobacterium tuberculosis* (56, 62). The reductive MU genome may also lack genes associated with copper toxicity recovery in Mmar, its evolutionary derivative (63). As a result of synergistic activity between antibiotics and metal ions (56, 62, 64), IE-nZeos may support the adaptation of lower dosage multidrug therapy.

Although we hypothesized that SA-macroGPs would adsorb MU better than their uncoated macroGP counterparts, both macroGPs and SA-macroGPs significantly adsorbed MU (Figure 5). MacroGPs and SA-macroGPs also adsorbed MRSA in significant quantities (21), implying potential broad-spectrum adsorptive activity that may benefit treatment of secondary infections of the Buruli ulcer (65, 66). These results may indicate either consistency in GP-binding motifs and/or GP pore sizes (Figure 1) between bacteria or curtailed performance of SA-enriched GPs resulting from side group dissociation (21).

As a highly hydrophobic molecule, mycolactone was also anticipated to demonstrate greater adherence to PTES-GPs and SA-mesoGPs. Our mycolactone – mesoGP adsorption results parallel GP adhesion of MRSA α-hemolysin toxin (21). Though both SA-mesoGPs and non-coated mesoGPs adsorbed α-hemolysin, SA-coated GPs demonstrated a modestly enhanced binding compared to uncoated GPs (21). Despite the greater hydrophobicity of PTES-GPs, the aromatic ring structure of this coating may have produced greater steric hindrance (67) than the fatty acid chain of the SA-GPs coating. Future studies may seek to establish longitudinal surface group stability and identify target-specific GP binding domains.

One of the greatest obstacles to effective MU treatment is the discordance between *in vitro* and *in vivo* susceptibility to small molecule compounds. Because IE-nZeos and GPs demonstrate antimicrobial and adsorptive activities *in vitro*, their unconventional antimicrobial mechanisms warrant further investigation for activity *in vivo*. As topical treatments, aluminosilicates offer the potential to physically protect mycobacterial skin and soft tissue wounds and provide antimicrobial and mycolactone adsorptive therapy for individuals with Buruli ulcer or Mmar infections.

Data availability statement

The original contributions presented in the study are included in the article/supplementary material. Further inquiries can be directed to the corresponding author.

Author contributions

D-KS and SH conceived and supervised the research. RD, JP, SC, D-KS, and SH designed the experiments. RD, FA, JP, and SC performed the experiments. All authors analyzed the experimental results and participated in writing and editing the manuscript. All authors contributed to the article and approved the submitted version.

Funding

This research was supported by funds from the National Institutes of Health R21AI121733 to D-KS and SH.

Acknowledgments

We acknowledge the use of facilities within the Eyring Materials Center at Arizona State University supported in part by NNCI-ECCS-2025490. FA was supported in part by funds from the School of Life Sciences Undergraduate Research (SOLUR) Program.

Conflict of interest

The authors declare that the research was conducted in the absence of any commercial or financial relationships that could be construed as a potential conflict of interest.

Publisher's note

References

1. Portaels F, Johnson P, Meyers WM. *Diagnosis of Mycobacterium ulcerans disease: a manual for health care providers*. Geneva (CH): World Health Organization (2001).

2. Wallace JR, Mangas KM, Porter JL, Marcsisin R, Pidot SJ, Howden B, et al. *Mycobacterium ulcerans* low infectious dose and mechanical transmission support insect bites and puncturing injuries in the spread of buruli ulcer. *PloS Negl Trop Diseases.* (2017) 11(4):e0005553. doi: 10.1371/journal.pntd.0005553

3. Portaels F, Meyers WM, Ablordey A, Castro AG, Chemlal K, de Rijk P, et al. First cultivation and characterization of *Mycobacterium ulcerans* from the environment. *PloS Negl Trop Dis* (2008) 2(3):e178. doi: 10.1371/journal.pntd.0000178

4. Zingue D, Panda A, Drancourt M. A protocol for culturing environmental strains of the buruli ulcer agent, *Mycobacterium ulcerans*. *Sci Rep* (2018) 8(1):6778. doi: 10.1038/s41598-018-25278-y

5. Zingue D, Bouam A, Tian RBD, Drancourt M. Buruli ulcer, a prototype for ecosystem-related infection, caused by *Mycobacterium ulcerans*. *Clin Microbiol Rev* (2018) 31(1):e00045–17. doi: 10.1128/CMR.00045-17

6. Sarfo FS, Phillips RO, Rangers B, Mahrous EA, Lee RE, Tarelli E, et al. Detection of mycolactone A/B in *Mycobacterium ulcerans*–infected human tissue. *PloS Negl Trop Diseases.* (2010) 4(1):e577. doi: 10.1371/journal.pntd.0000577

7. George KM, Chatterjee D, Gunawardana G, Welty D, Hayman J, Lee R, et al. Mycolactone: a polyketide toxin from *Mycobacterium ulcerans* required for virulence. *Science* (1999) 283(5403):854–7. doi: 10.1126/science.283.5403.854

8. En J, Goto M, Nakanaga K, Higashi M, Ishii N, Saito H, et al. Mycolactone is responsible for the painlessness of *Mycobacterium ulcerans* infection (Buruli ulcer) in a murine study. *Infect Immun* (2007) 76(5):2002-2007. doi: 10.1128/IAI.01588-07

9. Houngbédji GM, Bouchard P, Frenette J. *Mycobacterium ulcerans* infections cause progressive muscle atrophy and dysfunction, and mycolactone impairs satellite cell proliferation. *Am J Physiol Regul Integr Comp Physiol* (2011) 300(3): R724–32. doi: 10.1152/ajpregu.00393.2010

10. Gomez JE, Mckinney JD. *M. tuberculosis* persistence, latency, and drug tolerance. *Tuberculosis* (2004) 84(1-2):29–44. doi: 10.1016/j.tube.2003.08.003

11. Kibadi K, Tsakala M, Mputu-Yamba JB, Muyembe T, Kashongwe M, Imposso B, et al. [Buruli ulcer in angolese refugees in the Kimpese area, lower Congo, D.R. Congo]. *Sante* (2003) 13(1):39–41.

12. Van Der Werf TS, Barogui YT, Converse PJ, Phillips RO, Stienstra Y. Pharmacologic management of *Mycobacterium ulcerans* infection. *Expert Rev Clin Pharmacol* (2020) 13(4):391–401. doi: 10.1080/17512433.2020.1752663

13. Klis S, Ranchor A, Phillips RO, Abass KM, Tuah W, Loth S, et al. Good quality of life in former buruli ulcer patients with small lesions: long-term follow-up of the BURULICO trial. *PloS Negl Trop Diseases.* (2014) 8(7):e2964. doi: 10.1371/journal.pntd.0002964

14. Klis S, Stienstra Y, Phillips RO, Abass KM, Tuah W, van der Werf TS. Long term streptomycin toxicity in the treatment of buruli ulcer: follow-up of participants in the BURULICO drug trial. *PloS Negl Trop Diseases.* (2014) 8(3): e2739. doi: 10.1371/journal.pntd.0002739

15. Stevens DL, Bisno AL, Chambers HF, Dellinger EP, Goldstein EJC, Gorbach SL, et al. Practice guidelines for the diagnosis and management of skin and soft tissue infections: 2014 update by the Infectious Diseases Society of America. *Clin Infect Diseases.* (2014) 59(2):e10–52. doi: 10.1093/cid/ciu296

16. Adusumilli S, Haydel SE. *In vitro* antibacterial activity and *in vivo* efficacy of hydrated clays on *Mycobacterium ulcerans* growth. *BMC Complementary Altern Med* (2015) 16(1). doi: 10.1186/s12906-016-1020-5

17. WHO Advisory Group on Buruli Ulcer. *Report of the 6th WHO advisory group meeting on buruli ulcer*. WHO headquarters, Geneva, Switzerland. Geneva (CH): World Health Organization (2003).

18. Provis JL. Geopolymers and other alkali activated materials: why, how, and what? *Materials Structures* (2014) 47(1-2):11–25. doi: 10.1617/s11527-013-0211-5

19. Otto CC, Haydel SE. Exchangeable ions are responsible for the *in vitro* antibacterial properties of natural clay mixtures. *PloS One* (2013) 8(5):e64068. doi: 10.1371/journal.pone.0064068

20. Morrison KD, Misra R, Williams LB. Unearthing the antibacterial mechanism of medicinal clay: a geochemical approach to combating antibiotic resistance. *Sci Rep* (2016) 6(1):19043. doi: 10.1038/srep19043

21. Popovich J, Chen S, Iannuzo N, Ganser C, Seo D-K, Haydel SE. Synthesized geopolymers adsorb bacterial proteins, toxins, and cells. *Front Bioengineering Biotechnol* (2020) 8. doi: 10.3389/fbioe.2020.00527

22. Chen S, Popovich J, Zhang W, Ganser C, Haydel SE, Seo D-K. Superior ion release properties and antibacterial efficacy of nanostructured zeolites ion-exchanged with zinc, copper, and iron. *RSC Advances.* (2018) 8(66):37949–57. doi: 10.1039/C8RA06556J

23. Chen S, Popovich J, Iannuzo N, Haydel SE, Seo D-K. Silver-ion-exchanged nanostructured zeolite X as antibacterial agent with superior ion release kinetics and efficacy against methicillin-resistant *Staphylococcus aureus*. *ACS Appl Materials Interfaces* (2017) 9(45):39271–82. doi: 10.1021/acsami.7b15001

24. Otto C, Haydel S. Microbicidal clays: composition, activity, mechanism of action, and therapeutic applications. In: Méndez-Vilas A, editor. *Microbial pathogens and strategies for combating them: science, technology and education*, vol. 2 . Badajoz, Spain: Formatex Research Center (2013). p. 1169–80.

25. Coelho TS, Halicki PCB, Silva L, Menezes Vicenti JR, Gonçalves BL, Almeida Da Silva PE, et al. Metal-based antimicrobial strategies against intramacrophage *Mycobacterium tuberculosis*. *Lett Appl Microbiol* (2020) 71 (2):146–53. doi: 10.1111/lam.13298

26. Chen S, Zhang W, Sorge LP, Seo D-K. Exploratory synthesis of low-silica nanozeolites through geopolymer chemistry. *Crystal Growth Design.* (2019) 19 (2):1167–71. doi: 10.1021/acs.cgd.8b01636

27. Hashish E, Merwad A, Elgaml S, Amer A, Kamal H, Elsadek A, et al. *Mycobacterium marinum* infection in fish and man: epidemiology, pathophysiology and management; a review. *Veterinary Quarterly.* (2018) 38 (1):35–46. doi: 10.1080/01652176.2018.1447171

28. Pidot SJ, Asiedu K, Käser M, Fyfe JAM, Stinear TP. *Mycobacterium ulcerans* and other mycolactone-producing mycobacteria should be considered a single species. *PloS Negl Trop Diseases*. (2010) 4(7):e663. doi: 10.1371/journal.pntd.0000663

29. Haydel SE, Remenih CM, Williams LB. Broad-spectrum *in vitro* antibacterial activities of clay minerals against antibiotic-susceptible and antibiotic-resistant bacterial pathogens. *J Antimicrobial Chemotherapy.* (2007) 61 (2):353–61. doi: 10.1093/jac/dkm468

30. Jernigan JA, Farr BM. Incubation period and sources of exposure for cutaneous *Mycobacterium marinum* infection: case report and review of the literature. *Clin Infect Diseases.* (2000) 31(2):439–43. doi: 10.1086/313972

31. Franco-Paredes C, Marcos LA, Henao-Martínez AF, Rodríguez-Morales AJ, Villamil-Gómez WE, Gotuzzo E, et al. Cutaneous mycobacterial infections. *Clin Microbiol Rev* (2018) 32(1):e00069–18. doi: 10.1128/CMR.00069-18

32. Johnson MG, Stout JE. Twenty-eight cases of *Mycobacterium marinum* infection: retrospective case series and literature review. *Infection* (2015) 43(6):655–62. doi: 10.1007/s15010-015-0776-8

33. Prasanna AN, Mehra S. Comparative phylogenomics of pathogenic and non-pathogenic mycobacterium. *PloS One* (2013) 8(8):e71248. doi: 10.1371/journal.pone.0071248

34. Tăbăran A-F, Matea CT, Mocan T, Tăbăran A, Mihaiu M, Iancu C, et al. Silver nanoparticles for the therapy of tuberculosis. *Int J Nanomedicine* (2020) 15:2231–58. doi: 10.2147/IJN.S241183

35. Mohanty S, Jena P, Mehta R, Pati R, Banerjee B, Patil S, et al. Cationic antimicrobial peptides and biogenic silver nanoparticles kill mycobacteria without eliciting DNA damage and cytotoxicity in mouse macrophages. *Antimicrobial Agents Chemotherapy.* (2013) 57(8):3688–98. doi: 10.1128/AAC.02475-12

36. Geroult S, Phillips RO, Demangel C. Adhesion of the ulcerative pathogen *Mycobacterium ulcerans* to DACC-coated dressings. *J Wound Care* (2014) 23 (8):417–24. doi: 10.12968/jowc.2014.23.8.417

37. Bowler PG, Welsby S, Towers V. *In vitro* antimicrobial efficacy of a silver-containing wound dressing against mycobacteria associated with atypical skin ulcers. *Wounds* (2013) 25(8):225–30.

38. Medpelli D, Seo J-M, Seo D-K. Geopolymer with hierarchically meso-/macroporous structures from reactive emulsion templating. *J Am Ceramic Society.* (2014) 97(1):70–3. doi: 10.1111/jace.12724

39. Kriven WM, Bell J, Gordon M. Geopolymer refractories for the glass manufacturing industry. In: *64th Conference on Glass Problems: Ceramic Engineering and Science Proceedings*. (2004) Wiley Online Library. 25 (1):57–79. doi: 10.1002/9780470294857.ch5

40. Adusumilli S, Mve-Obiang A, Sparer T, Meyers W, Hayman J, Small PLC. *Mycobacterium ulcerans* toxic macrolide, mycolactone modulates the host immune response and cellular location of m. ulcerans in vitro and *in vivo*. *Cell Microbiol* (2005) 7(9):1295–304. doi: 10.1111/j.1462-5822.2005.00557.x

41. Demangel C, Stinear TP, Cole ST. Buruli ulcer: reductive evolution enhances pathogenicity of *Mycobacterium ulcerans*. *Nat Rev Microbiol* (2009) 7(1):50–60. doi: 10.1038/nrmicro2077

42. Duxson P, Provis JL, Lukey GC, Mallicoat SW, Kriven WM, Van Deventer JSJ. Understanding the relationship between geopolymer composition, microstructure and mechanical properties. *Colloids Surfaces A: Physicochemical Eng Aspects* (2005) 269(1-3):47–58. doi: 10.1016/j.colsurfa.2005.06.060

43. Scherr N, Pluschke G, Thompson CJ, Ramón-García S. Selamectin is the avermectin with the best potential for buruli ulcer treatment. *PloS Negl Trop diseases*. (2015) 9(8):e0003996. doi: 10.1371/journal.pntd.0003996

44. Al-Ani A, Freitas C, Zholobenko V. Nanostructured large-pore zeolite: The enhanced accessibility of active sites and its effect on the catalytic performance. *Microporous Mesoporous Materials*. (2020) 293:109805. doi: 10.1016/j.micromeso.2019.109805

45. Scherr N, Gersbach P, Dangy J-P, Bomio C, Li J, Altmann K-H, et al. Structure-activity relationship studies on the macrolide exotoxin mycolactone of *Mycobacterium ulcerans*. *PloS Negl Trop Dis* (2013) 7(3):e2143. doi: 10.1371/journal.pntd.0002143

46. Daffé M, Lanéelle MA, Lacave C. Structure and stereochemistry of mycolic acids of *Mycobacterium marinum* and *Mycobacterium ulcerans*. *Res Microbiol* (1991) 142(4):397–403. doi: 10.1016/0923-2508(91)90109-N

47. Barrett EP, Joyner LG, Halenda PP. The determination of pore volume and area distributions in porous substances. i. computations from nitrogen isotherms. *J Am Chem Society*. (1951) 73(1):373–80. doi: 10.1021/ja01145a126

48. Woods GL, Brown-Elliott BA, Conville PS, Desmond EP, Hall GS, Lin G, et al *M24-A2: Susceptibility testing of mycobacteria, nocardiae, and other aerobic actinomycetes*. Wayne (PA): Clinical Laboratory Standard Institute (2011).

49. Gunawardana G, Chatterjee D, George KM, Brennan P, Whittern D, Small PLC, et al. Characterization of novel macrolide toxins, mycolactones A and B, from a human pathogen, *Mycobacterium ulcerans*. *J Am Chem Soc* (1999) 121(25):6092–3. doi: 10.1021/ja9900171

50. Cadapan LD, Arslanian RL, Carney JR, Zavala SM, Small PL, Licari P. Suspension cultivation of *Mycobacterium ulcerans* for the production of mycolactones. *FEMS Microbiol Letters*. (2001) 205(2):385–9. doi: 10.1111/j.1574-6968.2001.tb10977.x

51. Marion E, Prado S, Cano C, Babonneau J, Ghamrawi S, Marsollier L. Photodegradation of the *Mycobacterium ulcerans* toxin, mycolactones: considerations for handling and storage. *PloS One* (2012) 7(4):e33600. doi: 10.1371/journal.pone.0033600

52. Davidovits J. Geopolymers. *J thermal analysis*. (1991) 37(8):1633–56. doi: 10.1007/BF01912193

53. Lu Z-H, Mu Y-M, Wang B-A, Li X-L, Lu J-M, Li J-Y, et al. Saturated free fatty acids, palmitic acid and stearic acid, induce apoptosis by stimulation of ceramide generation in rat testicular leydig cell. *Biochem Biophys Res Commun* (2003) 303(4):1002–7. doi: 10.1016/S0006-291X(03)00449-2

54. Swathy JR, Sankar MU, Chaudhary A, Aigal S, Anshup, Pradeep T. Antimicrobial silver: An unprecedented anion effect. *Sci Rep* (2015) 4(1):7161. doi: 10.1038/srep07161

55. Macomber L, Imlay JA. The iron-sulfur clusters of dehydratases are primary intracellular targets of copper toxicity. *Proc Natl Acad Sci* (2009) 106(20):8344–9. doi: 10.1073/pnas.0812808106

56. Shah S, Dalecki AG, Malalasekera AP, Crawford CL, Michalek SM, Kutsch O, et al. 8-hydroxyquinolines are boosting agents of copper-related toxicity in mycobacterium tuberculosis. *Antimicrobial Agents Chemotherapy* (2016) 60 (10):5765–76. doi: 10.1128/AAC.00325-16

57. Rowland JL, Niederweis M. A multicopper oxidase is required for copper resistance in *Mycobacterium* tuberculosis. *J Bacteriol* (2013) 195(16):3724–33. doi: 10.1101/2021.03.11.434961

58. Viveiros M, Martins M, Rodrigues L, Machado D, Couto I, Ainsa J, et al. Inhibitors of mycobacterial efflux pumps as potential boosters for anti-tubercular drugs. *Expert Rev anti-infective Ther* (2012) 10(9):983–98. doi: 10.1586/eri.12.89

59. Neyrolles O, Wolschendorf F, Mitra A, Niederweis M. Mycobacteria, metals, and the macrophage. *Immunol Rev* (2015) 264(1):249–63. doi: 10.1111/imr.12265

60. Adams KN, Takaki K, Connolly LE, Wiedenhoft H, Winglee K, Humbert O, et al. Drug tolerance in replicating mycobacteria mediated by a macrophage-induced efflux mechanism. *Cell* (2011) 145(1):39–53. doi: 10.1016/j.cell.2011.02.022

61. Black PA, Warren RM, Louw GE, van Helden PD, Victor TC, Kana BD. Energy metabolism and drug efflux in *Mycobacterium tuberculosis*. *Antimicrobial Agents Chemotherapy* (2014) 58(5):2491–503. doi: 10.1128/AAC.02293-13

62. Dalecki AG, Haeili M, Shah S, Speer A, Niederweis M, Kutsch O, et al. Disulfiram and copper ions kill *Mycobacterium tuberculosis* in a synergistic manner. *Antimicrobial Agents Chemotherapy*. (2015) 59(8):4835–44. doi: 10.1128/AAC.00692-15

63. Stinear TP, Seemann T, Harrison PF, Jenkin GA, Davies JK, Johnson PDR, et al. Insights from the complete genome sequence of *Mycobacterium marinum* on the evolution of mycobacterium tuberculosis. *Genome Res* (2008) 18(5):729–41. doi: 10.1101/gr.075069.107

64. Agertt VA, Bonez PC, Rossi GG, Flores VDC, Siqueira FDS, Mizdal CR, et al. Identification of antimicrobial activity among new sulfonamide metal complexes for combating rapidly growing mycobacteria. *BioMetals* (2016) 29 (5):807–16. doi: 10.1007/s10534-016-9951-3

65. Amissah NA, Glasner C, Ablordey A, Tetteh CS, Kotey NK, Prah I, et al. Genetic diversity of *Staphylococcus aureus* in buruli ulcer. *PloS Negl Trop Diseases*. (2015) 9(2):e0003421. doi: 10.1371/journal.pntd.0003421

66. Ruf M-T, Chauty A, Adeye A, Ardant M-F, Koussemou H, Johnson RC, et al. Secondary buruli ulcer skin lesions emerging several months after completion of chemotherapy: paradoxical reaction or evidence for immune protection? *PloS Negl Trop Dis* (2011) 5(8):e1252. doi: 10.1371/journal.pntd.0001252

67. Lin W, Zheng J, Zhuo J, Chen H, Zhang X. Characterization of sol-gel ORMOSIL antireflective coatings from phenyltriethoxysilane and tetraethoxysilane: Microstructure control and application. *Surface Coatings Technology*. (2018) 345:177–82. doi: 10.1016/j.surfcoat.2018.01.059